Achieving Atomic Resolution Magnetic Dichroism by Controlling the Phase Symmetry of an Electron Probe

Ján Rusz,[1,*] Juan-Carlos Idrobo,[2] and Somnath Bhowmick[3]
[1]*Department of Physics and Astronomy, Uppsala University, P.O. Box 516, 75120 Uppsala, Sweden*
[2]*Center of Nanophase Materials Sciences, Oak Ridge National Laboratory, Oak Ridge, Tennessee 37831, USA*
[3]*Department of Materials Science and Engineering, Indian Institute of Technology, Kanpur 208016, India*

(Received 21 February 2014; revised manuscript received 7 May 2014; published 30 September 2014)

The calculations presented here reveal that an electron probe carrying orbital angular momentum is just a particular case of a wider class of electron beams that can be used to measure electron magnetic circular dichroism (EMCD) with atomic resolution. It is possible to obtain an EMCD signal with atomic resolution by simply breaking the symmetry of the electron probe phase distribution using the aberration-corrected optics of a scanning transmission electron microscope. The required phase distribution of the probe depends on the magnetic symmetry and crystal structure of the sample. The calculations indicate that EMCD signals utilizing the phase of the electron probe are as strong as those obtained by nanodiffraction methods.

DOI: 10.1103/PhysRevLett.113.145501 PACS numbers: 61.05.J-, 41.20.Jb, 41.85.-p, 42.50.Tx

The development of quantitative magnetic characterization techniques goes hand in hand with progress in nanotechnology. A terabit per square inch recording density [1,2] means that the area available for one bit is not larger than a square of size $25 \times 25\ \mathrm{nm}^2$, assuming bits arranged laterally. This pushes demands for magnetic measurements down to a few nm scale [3,4], approaching atomic resolution.

An attractive option for measuring magnetism at such high spatial resolutions is an experimental technique based on electron magnetic circular dichroism [5–15] (EMCD). Particularly, a great promise came recently from utilizing electron vortex beams (EVBs) [16–20] within an electron microscope. With EVBs, it should be possible to measure EMCD in the direction of the transmitted beam [19,21–26], which brings a substantial increase in signal-to-noise ratio compared to intrinsic EMCD measured in between Bragg spots [5,7,15]. However, obtaining isolated atomic-size EVBs that can be used for EMCD measurements has not yet been possible, although different electron optical setups have been proposed [18,27–31].

In this Letter, we show how EMCD signals can be measured with atomic resolution in the electron microscope at the transmitted beam without the necessity of producing electron probes carrying orbital angular momentum (OAM). The calculations presented here reveal that EVBs carrying OAM are just a particular case of a wider class of electron beams that can be used to measure EMCD signals. The key feature for obtaining magnetic dichroism with atomic resolution is the relation between the crystal structure, magnetic symmetry of the sample, and the distribution of the phase in the electron beam. The predicted strength of such an EMCD signal is about half of what was reported in the first EMCD experiment on an iron crystal using a parallel beam [5], but with the main difference that it achieves atomic spatial resolution. As a consequence, electron beams that can be obtained by aberration-corrected scanning transmission electron microscopes (STEMs) without additional apertures are predicted to detect nonzero EMCD signals at the transmitted beam.

The theoretical prediction is based on a two-beam model for convergent beam electron diffraction (CBED) in STEM, see Fig. 1. The two disks represent a transmitted beam and elastically scattered beam with Bragg vector $\mathbf{G} = (G, 0, 0)$. For simplicity, the model assumes only one Bragg-scattered beam, a situation with a single symmetry plane—i.e., the x axis. However, the results obtained here can easily be generalized to a situation with more Bragg-scattered beams and different symmetries.

Overlap of the two CBED disks means that two regions describing the elastically scattered beam wave function need to be considered. Region Ω_1 is such that, for wave

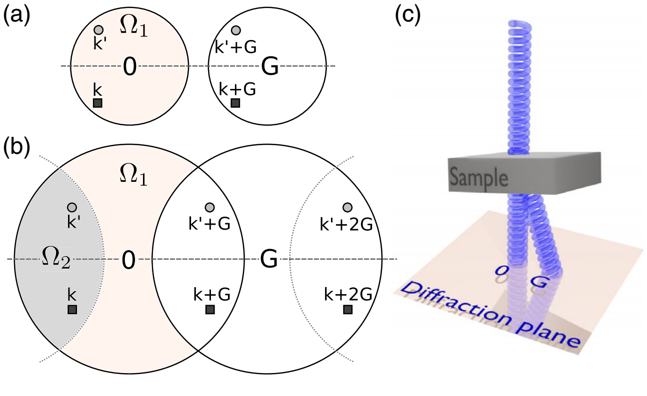

FIG. 1 (color online). Schematic drawing of a diffraction of a convergent electron beam assuming (a) no overlap between the CBED discs, (b) partial overlap of the CBED discs. Two-beam case orientation, illustrated in (c), is assumed and a general $\mathbf{k}$ vector is marked, together with its mirror image $\mathbf{k}'$. The mirror axis is marked as the dashed horizontal line.

vectors $\mathbf{k} \in \Omega_1$, there is no other wave vector within the same transmitted disk, which would differ from $\mathbf{k}$ by $\mathbf{G}$. Contrary to Ω_1, the shaded lens-shaped region Ω_2 in Fig. 1 contains wave vectors $\mathbf{k}$, for which $\mathbf{k}+\mathbf{G}$ lies within the same transmitted disk. Reasons for this distinction are related to the necessary condition for atomic resolution in STEM, which requires overlap of discs to achieve a coherent interference of beam components [32].

The wave function of the elastically scattered incoming probe can be written as

$$\psi_i(\mathbf{r}) = \sum_{\mathbf{k}\in\Omega_1\cup\Omega_2} Ce^{i\phi_{\mathbf{k}}} e^{i\mathbf{k}\cdot\mathbf{r}}[1+iT_{\mathbf{G}}e^{i\mathbf{G}\cdot\mathbf{r}}] + \sum_{\mathbf{k}\in\Omega_2} Ce^{i\phi_{\mathbf{k}+\mathbf{G}}} e^{i(\mathbf{k}+\mathbf{G})\cdot\mathbf{r}}[1+iT_{\mathbf{G}}e^{i\mathbf{G}\cdot\mathbf{r}}], \qquad (1)$$

where C is a real-valued normalization constant. The Bragg-scattered beam is phase shifted by $\pi/2$, and thus, its relative amplitude can be written as $iT_{\mathbf{G}}$ with real-valued $T_{\mathbf{G}}$. Both C and $T_{\mathbf{G}}$ are assumed to be $\mathbf{k}$ independent, which is a good approximation for thin samples usually studied in aberration-corrected STEM and spectrum imaging experiments [32]. The $\phi_{\mathbf{k}}$ represents the phase of the beam component with wave vector $\mathbf{k}$. Nonzero $\phi_{\mathbf{k}}$ can originate, for example, from aberrations or probe displacement. For an EVB with OAM $\langle \hat{L}_z \rangle = m\hbar$, we get $\phi_{\mathbf{k}} = m \arctan(k_y/k_x)$. Radius of the CBED disks $q_{\max}$ is related to convergence semiangle α via $\alpha = q_{\max}\lambda$, where λ is the de Broglie wavelength of electrons accelerated by voltage V_{acc}.

For the outgoing wave, the elastic scattering of the probe will be neglected. Additionally, the detector will be considered to be far away, observing a single plane wave $\psi_f(\mathbf{r}) = e^{i\mathbf{k}_f\cdot\mathbf{r}}$.

The double-differential scattering cross section can then be evaluated as (see Supplemental Material [33])

$$\begin{aligned}\frac{\partial^2\sigma}{\partial\Omega\partial E} = {}& C^2 \sum_{\mathbf{k}\in\Omega_1\cup\Omega_2} [S(\mathbf{q},\mathbf{q},E) + T_{\mathbf{G}}^2 S(\mathbf{q}-\mathbf{G},\mathbf{q}-\mathbf{G},E) + 2T_{\mathbf{G}}\mathrm{Im}[S(\mathbf{q},\mathbf{q}-\mathbf{G},E)]] \\ &+ \sum_{\mathbf{k}\in\Omega_2} C^2[[1+2T_{\mathbf{G}}\sin(\Delta\phi_{\mathbf{k},\mathbf{G}})]S(\mathbf{q}-\mathbf{G},\mathbf{q}-\mathbf{G},E) + T_{\mathbf{G}}^2 S(\mathbf{q}-2\mathbf{G},\mathbf{q}-2\mathbf{G},E) \\ &+ 2T_{\mathbf{G}}\mathrm{Im}[S(\mathbf{q}-\mathbf{G},\mathbf{q}-2\mathbf{G},E)] + 2\mathrm{Re}[e^{-i\Delta\phi_{\mathbf{k},\mathbf{G}}}S(\mathbf{q},\mathbf{q}-\mathbf{G},E)] \\ &+ 2T_{\mathbf{G}}\mathrm{Im}[e^{-i\Delta\phi_{\mathbf{k},\mathbf{G}}}S(\mathbf{q},\mathbf{q}-2\mathbf{G},E)] + 2T_{\mathbf{G}}^2\mathrm{Re}[e^{-i\Delta\phi_{\mathbf{k},\mathbf{G}}}S(\mathbf{q}-\mathbf{G},\mathbf{q}-2\mathbf{G},E)]], \qquad (2)\end{aligned}$$

where $\Delta\phi_{\mathbf{k},\mathbf{G}} = \phi_{\mathbf{k}+\mathbf{G}} - \phi_{\mathbf{k}}$, and

$$S(\mathbf{q},\mathbf{q}',E) = \sum_{I,F} \left\langle F \middle| \frac{e^{-i\mathbf{q}\cdot\mathbf{r}}}{q^2} \middle| I \right\rangle \left\langle I \middle| \frac{e^{i\mathbf{q}'\cdot\mathbf{r}}}{q'^2} \middle| F \right\rangle \delta(E - E_F + E_I), \qquad (3)$$

is the mixed dynamical form factor (MDFF), with momentum transfer $\mathbf{q} = \mathbf{k}_f - \mathbf{k}$ carrying the $\mathbf{k}$ dependence of the terms in the sum in Eq. (2). The $|I\rangle, |F\rangle$ denote initial and final states of crystal with energy E_I, E_F, respectively. Note that the Coulomb factors have been included directly into the definition of the MDFF.

Magnetic signal originates from imaginary parts of MDFFs according to the dipole model [15,35]

$$S(\mathbf{q},\mathbf{q}',E) \approx \frac{N(E)\mathbf{q}\cdot\mathbf{q}' + i(\mathbf{q}\times\mathbf{q}')\cdot\mathbf{M}(E)}{q^2 q'^2}, \qquad (4)$$

where $N(E)$ stands for an isotropic nonmagnetic white-line component and $\mathbf{M}(E)$ is a vector representing the magnetic component. Assuming magnetization only along the z direction and having $\mathbf{G} = (G,0,0)$, one obtains

$$\mathrm{Im}[S(\mathbf{q}-m\mathbf{G},\mathbf{q}-n\mathbf{G},E)] = \frac{(n-m)GM_z(E)q_y}{|\mathbf{q}-m\mathbf{G}|^2|\mathbf{q}-n\mathbf{G}|^2}. \qquad (5)$$

In the simplest case, when elastic scattering is neglected ($T_{\mathbf{G}} = 0$) and the convergence angle is small, i.e., $q_{\max} < (G/2)$ and, thus, Ω_2 is empty, Eq. (2) reduces to a simple sum of dynamical form factors $(\partial^2\sigma/\partial\Omega\partial E) = C^2\sum_{\mathbf{k}\in\Omega_1} S(\mathbf{q},\mathbf{q},E)$. In other words, Eq. (2) becomes an incoherent summation over all components $\mathbf{k}$ of the convergent electron probe. No magnetic signal can arise from such a condition because the dynamical form factor is real [see Eq. (5) for $n = m = 0$]. Notice that EMCD is defined as the result of subtracting two sets of electron energy-loss spectra collected with different electron phases [5]. If there is not a magnetic signal in the inelastic scattering, there would not be an EMCD signal either.

Assuming non-negligible elastic scattering (nonzero $T_{\mathbf{G}}$) for a probe with a small enough convergence angle, so that there is no overlap of the diffracted discs [empty Ω_2, see Fig. 1(a)], Eq. (2) reduces to the first sum only. The third term in the first sum explicitly contains an imaginary part of MDFF; i.e., one can expect a magnetic signal to be present at some scattering angles. However, there is no dependence of the scattering cross section on the phase $\phi_{\mathbf{k}}$, which means that the OAM, or in fact, any $\mathbf{k}$-space distribution of the phase in the probe does not matter. In other words, if the convergence angle is small enough such that $q_{\max} < (G/2)$, the beam vorticity does not influence the inelastic scattering cross section.

One can observe a magnetic signal in the setting described above, but the distribution of the magnetic signal is antisymmetric with respect to the mirror axes. Because the mirror axes necessarily pass through the transmitted beam, an EMCD signal cannot be observed by a detector centered on the transmitted beam, regardless of how large the collection angle is. An example of a CBED diffraction pattern calculated for an EVB with $q_{\max} < (G/2)$ is shown below in the left column of Fig. 3. The proof of an antisymmetry of EMCD signal proceeds in the following way: Let us consider a wave vector $\mathbf{k}' = (k_x, -k_y, k_z)$, which is a mirror image of the wave vector $\mathbf{k} = (k_x, k_y, k_z)$, see Fig. 1(a). Their combined contribution to the magnetic signal at $\mathbf{k}_f^{(1)} = (k_x^f, k_y^f, k_z^f)$ is evaluated using Eq. (5) as

$$2T_{\mathbf{G}} G M_z(E) \left[\frac{q_y}{|\mathbf{q}|^2 |\mathbf{q}-\mathbf{G}|^2} + \frac{q'_y}{|\mathbf{q}'|^2 |\mathbf{q}'-\mathbf{G}|^2} \right], \tag{6}$$

where $q_y = k_y^f - k_y$ and $q'_y = k_y^f + k_y$. Moving the detector orientation to its mirror image $\mathbf{k}_f^{(2)} = (k_x^f, -k_y^f, k_z^f)$ leads to

$$q_y^{(2)} = -k_y^f - k_y = -q'_y \rightarrow |\mathbf{q}^{(2)}| = |\mathbf{q}'|, \tag{7}$$

$$q'^{(2)}_y = -k_y^f + k_y = -q_y \rightarrow |\mathbf{q}'^{(2)}| = |\mathbf{q}|, \tag{8}$$

and similarly for $|\mathbf{q}-\mathbf{G}|$. The q_y and q'_y swap and change sign; i.e., the magnetic signal in Eq. (6) changes sign as well. This holds true for all $\mathbf{k}$ from the lower half-circles of the CBED disks; thus, an EMCD signal is, indeed, distributed antisymmetrically with respect to the mirror axis. In particular, it vanishes right at the symmetry axis. All observations of EMCD done so far, except for, possibly, Ref. [19], are of this nature—so called intrinsic EMCD, caused by coherence of elastically scattered beam components [5].

Next, we consider a situation with no elastic scattering ($T_{\mathbf{G}} = 0$), but $q_{\max} > (G/2)$. This can occur either for ultrathin samples and sufficiently large convergence angles, or when the unit cell is large (i.e., the reciprocal lattice vectors G are small). A limiting case is a single atom in a cell with an infinite lattice constant. Then, for any nonzero α, the $q_{\max} = \alpha/\lambda$ will be larger than $(G/2) = (1/2a) \rightarrow 0$.

The inelastic scattering cross section can be written as

$$\frac{\partial^2 \sigma}{\partial \Omega \partial E} = C^2 \sum_{\substack{\mathbf{k} \\ k_\perp < q_{\max}}} S(\mathbf{q}, \mathbf{q}, E) + 2C^2 \sum_{\mathbf{k} \in \Omega_2} \mathrm{Re}[e^{-i\Delta\phi_{\mathbf{k},\mathbf{G}}} S(\mathbf{q}, \mathbf{q}-\mathbf{G}, E)]. \tag{9}$$

There are two key findings: (1) the scattering cross section depends on the distribution of the phase in the beam wave front, (2) an EMCD signal can be observed, despite the fact that the elastic scattering of the probe was neglected. This time, however, the imaginary part of MDFF is multiplied by a sine function of $\Delta\phi_{\mathbf{k},G}$. A combined contribution of the probe component $\mathbf{k}$ and its mirror image $\mathbf{k}'$ is

$$2GM_z(E) \left[\frac{\sin(\Delta\phi_{\mathbf{k},\mathbf{G}}) q_y}{|\mathbf{q}|^2 |\mathbf{q}-\mathbf{G}|^2} + \frac{\sin(\Delta\phi_{k\prime,G}) q'_y}{|\mathbf{q}'|^2 |\mathbf{q}'-\mathbf{G}|^2} \right]. \tag{10}$$

Note that for a vortex beam passing directly through an atomic column $\Delta\phi_{\mathbf{k},G} = -\Delta\phi_{k\prime,G}$, which allows us to take the sine function out of the brackets together with a change of the plus sign into a minus sign in between the two terms. Moving the detector from $\mathbf{k}_f^{(1)}$ to its mirror image $\mathbf{k}_f^{(2)}$ transforms the momentum transfer vectors as in Eqs. (7) and (8)—both two terms change sign and then swap their order. But because of the minus sign in between them, the resulting contribution is the same at both detector orientations. This inelastic electron diffraction situation is very different from the previous case, because here there is a symmetric distribution of EMCD with respect to the mirror axis. A symmetric distribution of the magnetic signal allows us to detect EMCD at the transmitted beam. This result is in agreement with predictions of Refs. [22,24] and recent simulations [25].

The prediction can be illustrated by a simulation of the distributions of the nonmagnetic and magnetic contributions to the scattering cross section of a single Fe atom, Fig. 2. The Fe atom was placed in a cell of size $5.3 \times 5.3 \times 0.53$ nm^3. The simulations were done using a combined multislice—Bloch-wave approach described in Ref. [26], with the outgoing beam described as a single plane wave, and the incoming beam was an EVB with $\langle \hat{L}_z \rangle = 1\hbar$ and $q_{\max} = 0.1$ a.u.$^{-1}$, which at $V_{\mathrm{acc}} = 200$ kV means $\alpha = 4.7$ mrad.

The calculations indicate a symmetry of the distribution of magnetic signal in the diffraction plane, which is a consequence of $\Delta\phi_{\mathbf{k},G} = -\Delta\phi_{k\prime,G}$ for all pairs of $\mathbf{k}$ and $\mathbf{k}'$ connected by a mirror symmetry. If, instead, $\Delta\phi_{\mathbf{k},G} = \Delta\phi_{k\prime,G}$, the imaginary part term in Eq. (9) would not change sign and the resulting distribution of EMCD would be antisymmetric with respect to the mirror axis.

Thus, the key element to detect an EMCD signal with atomic resolution here is the $\mathbf{k}$-space distribution of the phase $\phi_{\mathbf{k}}$ in the electron probe. Basically, in STEM one simply needs to set a phase distribution of the electron

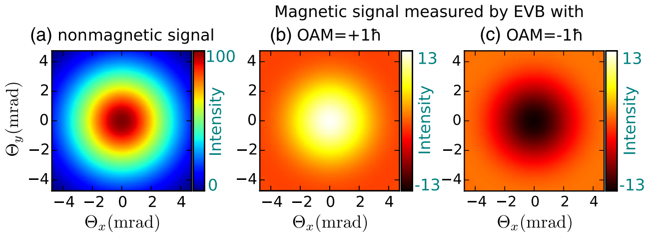

FIG. 2 (color online). L_3-edge energy-filtered diffraction pattern of an EVB scattering on a single Fe atom. The individual panels show the nonmagnetic and magnetic components (EVBs with OAM $= \pm 1\hbar$) of the inelastic scattering cross section assuming the Fe magnetic moment along the z axis. The EMCD signal results from subtracting the OAM $= +1\hbar$ from OAM $= -1\hbar$ magnetic components.

probe that maximizes the symmetric component of EMCD in the diffraction plane, which happens when the phase differences $\Delta\phi_{\mathbf{k},G}$ are antisymmetric. Note that shifting the STEM probe from the atomic column by $\mathbf{X}$ introduces a phase factor $e^{i\mathbf{k}\cdot\mathbf{X}}$, which modifies the phase distribution and, in general, also its symmetry. As a consequence, the EMCD signal intensity is reduced [26] if the electron probe is not at the center of an atomic column; see also the Supplemental Material [33].

For a single atom, there is a continuum of mirror axes passing through the atom. As a consequence, the optimal beam shape for EMCD is a vortex beam passing through the atom because it has an antisymmetric phase difference with respect to all mirror axes passing through its core.

For a crystal with a discrete set of mirror symmetries, there is a wider range of phase distributions in the probe wave front that are antisymmetric with respect to all mirror axes. This is illustrated below, where all the terms of Eq. (2) are considered.

When considering both an overlap of CBED disks ($q_{\max} > (G/2)$) and elastic scattering of the incoming electron probe ($T_{\mathbf{G}} \neq 0$), the inelastic scattering cross section contains several terms with an imaginary part of MDFF. Some of the terms are strictly antisymmetric and do not depend on $\Delta\phi_{\mathbf{k},\mathbf{G}}$, but other terms depend on a phase difference via the real and imaginary parts of the phase factor, $e^{-i\Delta\phi_{\mathbf{k},\mathbf{G}}}$, multiplying them. Thus, an optimum phase distribution in the wave front may be rather complicated and will depend on the particular crystal structure and magnetic symmetry via dynamical diffraction effects.

With EVBs, when an imaginary part of MDFF is multiplied by the real (imaginary) part of the phase factor, $e^{-i\Delta\phi_{\mathbf{k},\mathbf{G}}}$, it leads to an antisymmetric (symmetric) EMCD distribution, respectively. It is interesting to observe how the symmetric contribution develops as the convergence angle increases. This is illustrated in Fig. 3 and in Fig. 1 in the Supplemental Material [33] for a bcc iron crystal with $a = 2.87$ Å and the beam accelerated by 200 kV propagating along (001) zone axis. The overlap onsets when $q_{\max} > \frac{1}{2}G_{(110)}$, where $\mathbf{G} = (110)$ is the smallest allowed reflection in a bcc structure. Thus, $q_{\max}$ must be larger than $\frac{1}{2}(\sqrt{2}/a) = 0.1303$ a.u.$^{-1}$ so that the CBED discs will overlap and Ω_2 becomes nonempty. Integrating the distribution of the magnetic signal over a circular aperture of diameter 8.7 mrad leads to a zero magnetic signal for $q_{\max} \leq 0.13$ a.u.$^{-1}$ and nonzero above. Clearly, when the CBED discs do not overlap (Fig. 3, left column), the EMCD is antisymmetrically distributed with respect to all mirror axes—horizontal, vertical, and two diagonal ones—as anticipated. Above the onset of overlap, this antisymmetry is broken.

Note that for a discrete set of mirror symmetries, as in the case of a bcc crystal, it is easy to construct a beam with a phase distribution, which has antisymmetric phase differences $\Delta\phi_{\mathbf{k},\mathbf{G}}$ with respect to all of the four mirror axes, but which is not a vortex beam carrying OAM. For example, a fourfold astigmatism [32] has the required symmetry, because, for any $\mathbf{k}$, the $\phi_{\mathbf{k}}$ changes sign under mirror symmetry, see Fig. 4(a). An explicit calculation of the inelastic electron scattering reveals an EMCD signal distribution, which is, indeed, not antisymmetric, Fig. 4(b). A calculated STEM image of the magnetic signal from the Fe L_3 edge, Fig. 4(c), shows atomically resolved EMCD with maxima around positions with fourfold symmetry. The Fe L_3 signal for bcc iron integrated over a collection angle of 43 mrad centered on a transmitted beam presents an EMCD of relative intensity of about 1%. The strength of this EMCD signal is only about half of what it was reported in the first EMCD experiment [5], but with the main difference that it has atomic spatial resolution. Moreover, with this approach, one can use the full intensity of the electron beam because there is no need of a spiral [27,30] or fork aperture [18,19], which should result in better signal to noise ratio EMCD measurements than with EVBs [19].

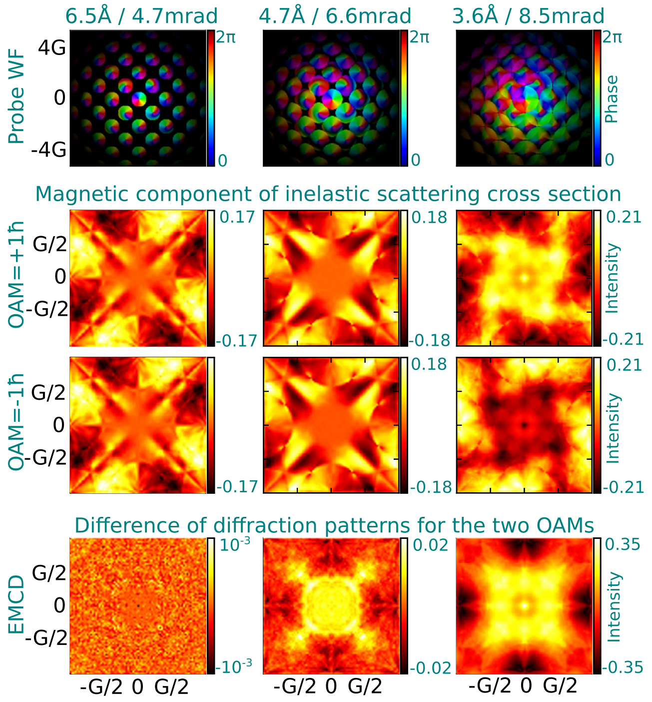

FIG. 3 (color online). Dependence of probe wave function and energy-filtered diffraction patterns on convergence angle. (Top row) Reciprocal space probe wave function after passing through 10 nm of bcc iron along (001) direction. Magnetic signal components of Fe-L_3 diffraction patterns for OAM of $\pm 1\hbar$ are shown in the middle rows. (Bottom row) Difference of magnetic signals for the two vorticities with OAM of $\pm 1\hbar$.

In conclusion, we show that a finite EMCD signal with atomic resolution can be observed at the transmitted beam without the necessity of using EVBs carrying OAM. The conditions necessary for EMCD are (1) a convergence angle large enough to cause an overlap of CBED disks and (2) a phase distribution of the probe in reciprocal space that is not invariant under mirror symmetries of the crystal. As a corollary, we propose a simple beam shape, which can be readily obtained in current aberration-corrected STEM

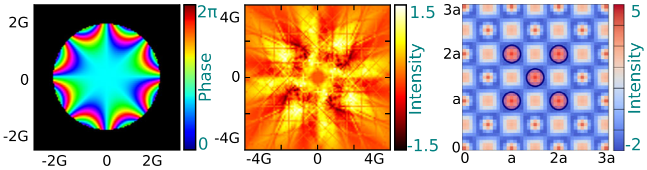

(a) probe WF (b) magnetic signal (c) STEM image of EMCD

FIG. 4 (color online). (a) Reciprocal space wave function (WF) of a beam distorted by fourfold astigmatism $C_{3,4b} = 0.1$ mm; $q_{\max} = 0.4$ a.u.$^{-1}$, $V_{\mathrm{acc}} = 200$ kV. (b) Magnetic component of the energy-filtered diffraction pattern at L_3 edge of iron, $G = 1/a$, $t = 10$ nm. (c) STEM spectrum image of the magnetic signal calculated with collection semiangle 43 mrad ($= 5G$). Atomic columns within one unit cell are marked by semitransparent red circles.

instruments, and which should allow us to measure EMCD at the transmitted beam. The EMCD signal obtained with the method presented can achieve atomic resolution and be as strong as EMCD nanodiffraction experiments. In a more general context, our work opens up new ways of utilizing aberration-correction electron optics to design atomic-size electron probes with tailored phase distributions for specific applications and/or crystal symmetries. These electron probes could be utilized to probe magnetic dichroism, optical dichroism, and the valley polarization of materials with unmatched spatial resolution.

J. R. acknowledges the Swedish Research Council and Swedish National Infrastructure for Computing (NSC center). J.-C. I. acknowledges support by the Center for Nanophase Materials Sciences (CNMS), which is sponsored at Oak Ridge National Laboratory by the Scientific User Facilities Division, Office of Basic Energy Sciences, U.S. Department of Energy. Comments by Peter M. Oppeneer and by the referee during the review process of this manuscript are gratefully acknowledged. S. B. acknowledges the support by IIT Kanpur new faculty initiation grant.

---

[*] Corresponding author.
jan.rusz@physics.uu.se

[1] J. K. W. Yang, Y. Chen, T. Huang, H. Duan, N. Thiyagarajah, H. K. Hui1, S. H. Leong, and V. Ng, Nanotechnology **22**, 385301 (2011).
[2] M. Mallary, A. Torabi, M. Benakli, IEEE Trans. Magn. **38**, 1719 (2002).
[3] T. P. Bigioni, X.-M. Lin, T. T. Nguyen, E. I. Corwin, T. A. Witten, and H. M. Jaeger, Nat. Mater. **5**, 265 (2006).
[4] S. Park, D. H. Lee, J. Xu, B. Kim, S. W. Hong, U. Jeong, T. Xu, and T. P. Russell, Science **323**, 1030 (2009).
[5] P. Schattschneider, S. Rubino, C. Hébert, J. Rusz, J. Kuneš, P. Novák, E. Carlino, M. Fabrizioli, G. Panaccione, and G. Rossi, Nature (London) **441**, 486 (2006).
[6] B. Warot-Fonrose, F. Houdellier, M. J. Hytch, L. Calmels, V. Serin, and E. Snoeck, Ultramicroscopy **108**, 393 (2008).
[7] P. Schattschneider, M. Stöger-Pollach, S. Rubino, M. Sperl, Ch. Hurm, J. Zweck, and J. Rusz, Phys. Rev. B **78**, 104413 (2008).
[8] Z. H. Zhang, X. F. Wang, J. B. Xu, S. Muller, C. Ronning, and Q. Li, Nat. Nanotechnol. **4**, 523 (2009).
[9] R. F. Klie, T. Yuan, M. Tanase, G. Yang, and Q. Ramasse, Appl. Phys. Lett. **96**, 082510 (2010).
[10] M. Stöger-Pollach, C. D. Treiber, G. P. Resch, D. A. Keays, and I. Ennen, Micron **42**, 456 (2011).
[11] Z. H. Zhang, H. L. Tao, M. He, and Q. Li, Scr. Mater. **65**, 367 (2011).
[12] J. Salafranca, J. Gazquez, N. Perez, A. Labarta, S. T. Pantelides, S. J. Pennycook, X. Batlle, and M. Varela, Nano Lett. **12**, 2499 (2012).
[13] B. Loukya, X. Zhang, A. Gupta, and R. Datta, J. Magn. Magn. Mater. **324**, 3754 (2012).
[14] Z. Q. Wang, X. Y. Zhong, R. Yu, Z. Y. Cheng, and J. Zhu, Nat. Commun. **4**, 1395 (2013).
[15] S. Muto, J. Rusz, K. Tatsumi, R. Adam, S. Arai, V. Kocevski, P. M. Oppeneer, D. E. Bürgler, and C. M. Schneider, Nat. Commun. **5**, 3138 (2014).
[16] K. Y. Bliokh, Y. P. Bliokh, S. Savelev, and F. Nori, Phys. Rev. Lett. **99**, 190404 (2007).
[17] M. Uchida and A. Tonomura, Nature (London) **464**, 737 (2010).
[18] B. J. McMorran, A. Agrawal, I. M. Anderson, A. A. Herzing, H. J. Lezec, J. J. McClelland, and J. Unguris, Science **331**, 192 (2011).
[19] J. Verbeeck, H. Tian, and P. Schattschneider, Nature (London) **467**, 301 (2010).
[20] J. Verbeeck, P. Schattschneider, S. Lazar, M. Stöger-Pollach, S. Löffler, A. Steiger-Thirsfeld, and G. Van Tendeloo, Appl. Phys. Lett. **99**, 203109 (2011).
[21] G. Van Tendeloo, S. Bals, S. Van Aert, J. Verbeeck, and D. Van Dyck, Adv. Mater. **24**, 5655 (2012).
[22] S. M. Lloyd, M. Babiker, and J. Yuan, Phys. Rev. Lett. **108**, 074802 (2012).
[23] J. Rusz and S. Bhowmick, Phys. Rev. Lett. **111**, 105504 (2013).
[24] J. Yuan, S. M. Lloyd, and M. Babiker, Phys. Rev. A **88**, 031801 (2013).
[25] P. Schattschneider, S. Löffler, M. Stöger-Pollach, and J. Verbeeck, Ultramicroscopy **136**, 81 (2014).
[26] J. Rusz, S. Bhowmick, M. Eriksson, and N. Karlsson, Phys. Rev. B **89**, 134428 (2014).
[27] J. Verbeeck, H. Tian, and A. Béché, Ultramicroscopy **113**, 83 (2012).
[28] P. Schattschneider, M. Stöger-Pollach, and J. Verbeeck, Phys. Rev. Lett. **109**, 084801 (2012).
[29] L. Clark, A. Béché, G. Guzzinati, A. Lubk, M. Mazilu, R. Van Boxem, and J. Verbeeck, Phys. Rev. Lett. **111**, 064801 (2013).
[30] K. Saitoh, Y. Hasegawa, N. Tanaka, and M. Uchida, Microscopy **61**, 171 (2012).
[31] O. L. Krivanek, J. Rusz, J.-C. Idrobo, T. J. Lovejoy, and N. Dellby, Microsc. Microanal. **20**, 832 (2014).
[32] S. J. Pennycook and P. D. Nellist, *Scanning Transmission Electron Microscopy: Imaging and Analysis* (Springer, New York, 2011), Chap. 2.
[33] See Supplemental Material at http://link.aps.org/supplemental/10.1103/PhysRevLett.113.145501, which includes Ref. [34], for a detailed derivation of Eq. (2), discussion of probe shift, and an additional figure.
[34] J. J. Sakurai and J. J. Napolitano, *Modern Quantum Mechanics* (Addison-Wesley, Reading, MA, 2010).
[35] J. Rusz, O. Eriksson, P. Novák, and P. M. Oppeneer, Phys. Rev. B **76**, 060408(R) (2007).